Endogenous Nanoparticles Strain Perovskite Host Lattice Providing Oxygen Capacity and Driving Oxygen Exchange and CH_4 Conversion to Syngas

Kalliopi Kousi,*[a] Dragos Neagu,*[a] Leonidas Bekris,[a] Evangelos I. Papaioannou[a] and Ian S. Metcalfe*[a]

Abstract: Particles dispersed on the surface of oxide supports have enabled a wealth of applications in electro- photo- and heterogeneous catalysis. Dispersing nanoparticles within the bulk of oxides is, however, synthetically much more challenging and therefore less explored, but could open new dimensions to control material properties analogous to substitutional doping of ions in crystal lattices. Here we demonstrate such a concept allowing extensive, controlled growth of metallic nanoparticles, at nanoscale proximity, within a perovskite oxide lattice as well as on its surface. By employing operando techniques, we show that in the emergent nanostructure, the endogenous nanoparticles and the perovskite lattice become reciprocally strained and seamlessly connected, enabling enhanced oxygen exchange. Additionally, even deeply embedded nanoparticles can reversibly exchange oxygen with a methane stream, driving its redox conversion to syngas with remarkable selectivity and long term cyclability while surface particles are present. These results not only exemplify the means to create extensive, self-strained nanoarchitectures with enhanced oxygen transport and storage capabilities, but also demonstrate that deeply submerged, redox-active nanoparticles could be entirely accessible to reaction environments, driving redox transformations and thus offering intriguing new alternatives to design materials underpinning several energy conversion technologies.

Introduction

Metallic nanoparticles dispersed on the surface of oxide supports have proven to be instrumental in controlling and tailoring the surface reactivity of materials for a wide variety of catalytic applications, especially in energy conversion technologies. However, what if nanoparticles could be dispersed within the bulk of materials rather than on their surface? How would such materials be made and what would be the impact on the material properties? A recent report shows that by assembling gold nanoparticles together with perovskite oxides (ABO_3) in a nanocomposite leads to strain within the perovskite oxide lattice, enhancing oxide ion transport and oxygen reduction activity[1]. Similarly, embedding noble metal nanoparticles within other inorganic crystal lattices enhances electronic transport in a manner analogue to substitutional doping[2]. Therefore, embedding metallic nanoparticles within non-metallic crystal lattices could open new possibilities to tailor materials , in particular through strain engineering, which has been shown to control multiple properties including oxide ion, electron and thermal transport[3–5], catalytic reactivity[3,6–9] and magnetic properties[10].

However, producing and controlling such nanocomposites remains challenging. Currently, these are being prepared by assembling metallic nanoclusters together with the non-metallic host lattice. However, this approach is limited to using a combination of metals (usually noble metals) and host lattices that do not interact chemically during preparation[1,11] posing fundamental limitations over the type of materials and nanostructures that can be achieved. An alternative would be to prepare such composites through a controlled disassembly process instead. The atoms which are meant to form the embedded phase would be initially dispersed as ions within the host lattice, as a solid solution, and upon reduction precipitated out of the lattice. Redox exsolution is one such process, employed for dispersing confined, partly submerged metallic nanoparticles on the surface of oxides. Exsolved nanoparticles display improved resistance to carbon deposition and agglomeration and enhanced activity due to strain[12,13], being extensively applied in electrochemical and catalytic processes[14–21].

Here we employ the exsolution concept outside its conventional use to homogenously grow metallic particles throughout the bulk of perovskite oxides of 100-150 μm particle size (Fig. 1). We show that the high dispersion achieved through this approach yields nanoparticles within nanoscale proximity to each other, inducing strain in both the metal and host lattices. In turn, this greatly enhances oxygen exchange across the nanocomposite, seamlessly connecting even the deepest embedded particles to the gas phase environment. Moreover, we show that the embedded nanoparticles can undergo cyclic, redox transformation between metal and metal oxide state, acting as readily accessible nanoscale reservoirs for oxygen storage, maintaining nanocomposite integrity and remain protected against agglomeration or other deactivation processes. Such unique combination of high oxygen transport, high oxygen storage capacity as well as redox robustness, makes these materials appealing for energy conversion technologies that rely on cyclic oxygen storage such thermochemical solar to fuel[22], redox flow batteries[23] and chemical looping[24]. To illustrate the applicability of our concept, we employ it towards the challenging process of CH_4 activation and conversion[25,26] via chemical looping partial oxidation (CLPO). In this process, the oxygen carrier material which reacts cyclically with a reducing and an oxidizing stream also needs to fulfil the catalytic role of CH_4 activation[27–30]. We exemplify this by using a titanate perovskite

[a] Dr. K. Kousi, Dr. D. Neagu, B.Eng. L. Bekris, Dr. E. I. Papaioannou, Prof. I. S. Metcalfe
School of Engineering
Newcastle University
Merz Court, NE1 7RU
E-mail: kalliopi.kousi@ncl.ac.uk, dragos.neagu@ncl.ac.uk, ian.metcalfe@ncl.ac.uk

Supporting information for this article is given via a link at the end of the document.

oxide ($La_{0.8}Ce_{0.1}Ni_{0.4}Ti_{0.6}O_3$), which is traditionally not ideal for such applications due to low surface area and low oxygen exchange capability[31]. However, upon the formation of surface and bulk metallic nanoparticles (Fig. 2a), this becomes very active for the process, producing synthesis gas with high selectivity and minimal carbon deposition at lower temperatures than conventional materials[32].

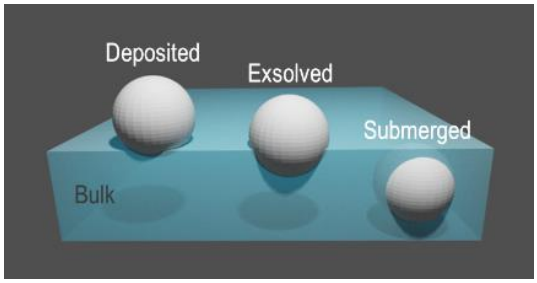

Figure 1. Controlling particle immersion with different preparation methods.

Results and Discussion

A perovskite oxide with endogenous nanoparticles

In order to promote bulk as opposed to surface exsolution, we introduce a set of design principles. We select a titanate perovskite with relatively low cation transport capabilities[33] in order to favour local particle nucleation as opposed to transport of the exsolvable ions to the surface. We introduce slight A-site deficiency in conjunction with relatively high B-site substitution (0.4 Ni in $La_{0.8}Ce_{0.1}Ni_{0.4}Ti_{0.6}O_3$ is equivalent to 10 wt.% Ni) to promote exsolution and increase the likelihood of metal nucleation throughout the perovskite lattice. Additionally, in order to overcome the relatively high energy barriers associated with nucleation and growth within an oxide lattice (arising from strain and oxide lattice reconstruction around the particle)[34,35], we increase the temperature and/or duration at which the exsolution process is carried out.

The synthesized perovskite displays high degree of crystallinity (illustrated by sharp peaks in X-ray diffraction patterns, Fig.2b and S1) and a particle size of 80-160 μm (Fig. S2). Figures 2c, 2d, 2i, S3 show that in such conditions the exsolution process still occurs in a controlled manner, producing homogenously dispersed particles on the surface and within the bulk. This is also reflected in the XRD pattern which indicates the presence of a main, remnant perovskite phase, henceforth referred to as $rABO_3$, a Ni metal phase peak and reflections associated with La_2TiO_5 which formed due to the extensive degree of exsolution achieved in this case (almost all the substituted Ni was exsolved, about 0.35 Ni out of the 0.4 in $La_{0.8}Ce_{0.1}Ni_{0.4}Ti_{0.6}O_3$, Supp. Note 1).

Close examination of this system revealed that the particles exsolved on the surface and in the bulk display key fundamental differences in terms of size, population, unit cell parameter and experienced strain. First, the particles exsolved in the bulk are much smaller as compared to the ones on the surface, approximately 13 vs 45 nm. This is probably due to the strain associated to particles growing within the bulk which, according to theoretical calculations is expected to be easier to accommodate for smaller particles[34,35]. Secondly, they are also more numerous, 1000 vs 100 particles per μm^2 respectively (Fig 2f, 2g, S4). It is worth noting that at these tremendously high population densities, the bulk particles are in nanoscale proximity of each other, maximising the strain they can exert on the host perovskite lattice. Indeed, the interparticle distance is of the same order of length size as the particles themselves (~13 and ~33 nm, respectively), as derived from a Voronoi tessellation of their spatial arrangement (Fig 2e, 2h, S4). Notably, as compared to standard Ni metal (3.5168 Å), surface particles are expansively strained by 0.29% (3.5272 Å), while the ones in the bulk are, not surprisingly, even more strained, at 0.37% (3.5301 Å). The high bulk particle population also induces microstrain in the remnant perovskite matrix $rABO_3$, roughly twice as high as compared to the initial perovskite (see peak broadening in Fig 2b and strain analysis in Fig. S5).

This striking difference in size and population between surface and bulk particles is also reflected in the shape of the Ni peak in the X-ray synchrotron diffraction pattern (Fig. 2f). The peak consists of a sharp tip (larger, surface particles) and broad base (smaller, bulk particles). The size-peak correspondence was also confirmed by chemically removing the particles at the surface, which also removes the sharp component of the Ni peak (Fig. S6). Quantification by Rietveld refinement from X-ray data revealed that overall the system exsolved ~8 wt.% Ni metal (corresponding to almost all the substituted Ni exsolving, 0.35 mol Ni per mol $rABO_3$), out of which 85% corresponds to the particles located within the bulk (Fig. S5). Overall, this system can be visualised as comprising of 1 wt.% of 45 nm Ni particles dispersed on the surface and 7 wt.% of 13 nm Ni particles dispersed within the bulk. This high ratio of bulk/surface exsolved particles is consistent with our design principle of maximising particle formation within the bulk as opposed to the surface.

Overall, the design employed here enables the creation of a self-nanostructured, self-strained composite system at the macroscale, which is expected to exhibit emergent properties[36,37], including enhanced bulk oxygen transport and therefore enable the connection between the bulk particles and the gas stream.

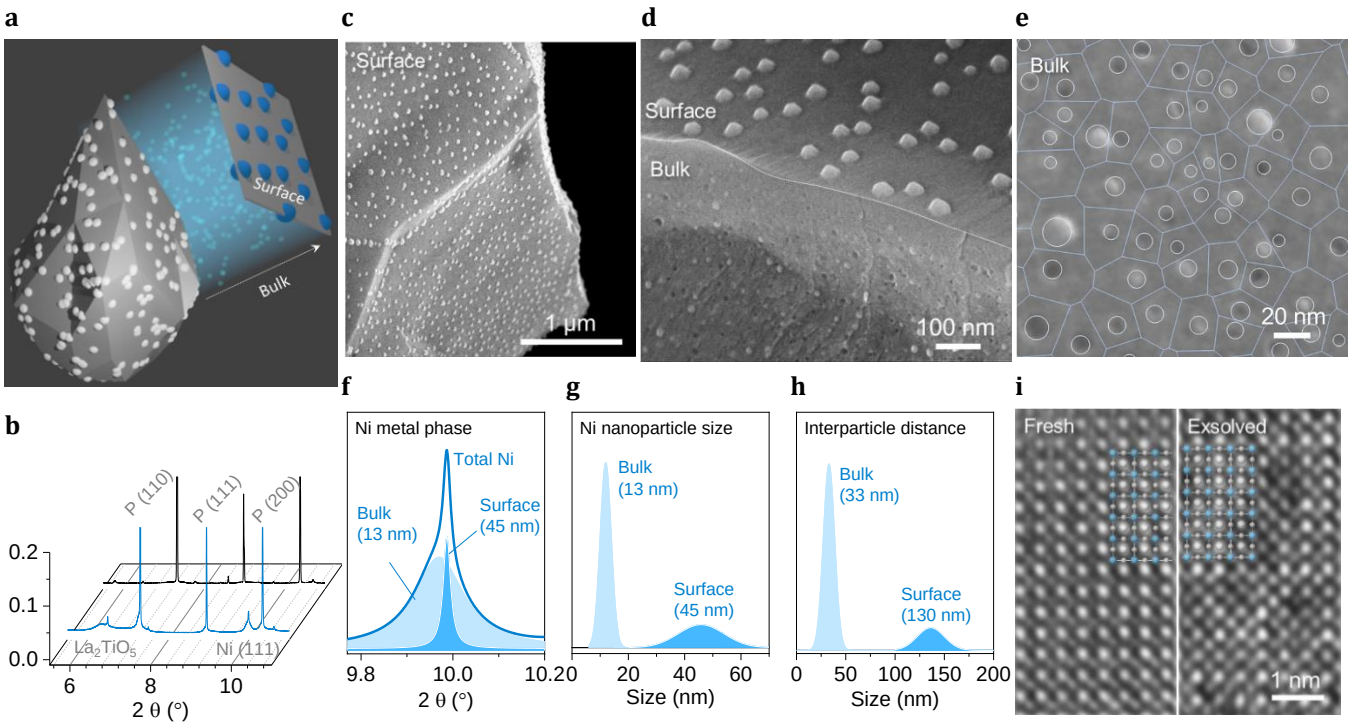

Figure 2. A system with submerged particles. (**a**) 3D model of a catalyst particle with nanoparticles dispersed on its surface and within its bulk. (**b**) Room temperature XRD patterns of $La_{0.8}Ce_{0.1}Ni_{0.4}Ti_{0.6}O_3$, in as-prepared state (black) and after exsolution at 1000 °C (10 h) in H_2 (blue). Both diffractograms are normalised on a scale from 0 to 1 (see Fig. S1 for details). (**c**)-(**d**) SEM micrographs showing: (**c**) an overview of the surface of the perovskite after exsolution. (**d**) Cross-section view after exsolution revealing surface and bulk particles. (**e**) Detail of the particles exsolved in the bulk (statistically half of the particles are missing due to the fact that the bulk was cleaved in order to acquire the image). The micrograph is superimposed with a corresponding Voronoi tessellation highlighting a virtual partitioning of the perovskite bulk into nanodomains associated to each particle exsolved within it. (**f**) Ni metal peak from b deconvoluted into surface and bulk particles contribution using Rietveld refinement. (**g**) Ni metal particle size distribution of d calculated by image analysis. (**h**) Domain size distribution calculated by image analysis on the Voronoi diagram in e (see Fig. S4 for additional information). (**i**) TEM images of the perovskite lattice before (left) and after exsolution (right); superimposed are the lattice models highlighting the expansion of the perovskite unit cell after reduction.

Controlling endogenous nanoparticles, strain and oxygen exchange

By employing different temperatures and durations for the reduction of the perovskite, the degree of the embedded metal loading, but most importantly, the size and interparticle distance of the embedded particles can be easily controlled. A series of such samples, ranging from a sample with no embedded particles (only surface particles) to samples with increasingly higher bulk metal nanoparticles content are shown in Fig. 3. It appears that the temperature controls the interparticle distance (smaller at lower temperatures), while duration controls size (larger with increasing time). From the phase and microstructure analysis shown in Fig. 3a-c it is evident that bulk particles emerge even at the lower reduction temperature of 900 °C, given enough time, and overall their weight fraction always dominates the contribution coming from the surface particles (compare Ni_S and Ni_B in Fig. 3f). In the prepared range of samples, the size of the embedded particles varies from ~3.5 to ~6.5 and to ~13 nm, while the corresponding interparticle distance varies from ~20 to ~25 and to ~33 nm, respectively (Fig. 3f, S7). At the same time, the particle size and population at the surface of these samples are very similar (Fig. S7).

In order to understand the effect of these parameters on oxygen exchange as well as oxygen capacity, we measured the oxygen uptake during oxidation of these samples. Since the characteristics of the surface particles are similar across these samples, it can be assumed that the surface exchange kinetics are similar and therefore the oxygen uptake experiments will reflect relative oxygen diffusivities within the bulk. As shown in Fig 3d, the sample only having surface particles displays a very low oxygen exchange rate and low oxygen capacity characteristic of a perovskite titanate system. As the embedded metal content is increased, both the oxygen capacity and oxygen exchange rate increase dramatically while the temperature at which oxygen exchange initiates decreases.

In order to quantify these effects, we fit the oxygen uptake measurement with a logistic law (characteristic of such oxidation processes – Eq. 18, Fig. S8) and plot the corresponding oxygen capacity (ζ_G, mol O per mol perovskite) and time constants (τ, h^{-1}) associated with oxygen exchange rate in Fig. 3f. It is apparent from this figure that, as expected, the oxygen capacity scales proportionally with the metal content (compare Ni_B and ζ_G in Fig. 3f). On the contrary, the rate of oxygen exchange does not seem to correlate with the embedded metal content (compare Ni_B and τ in Fig. 3f), but seems to correlate much more strongly with

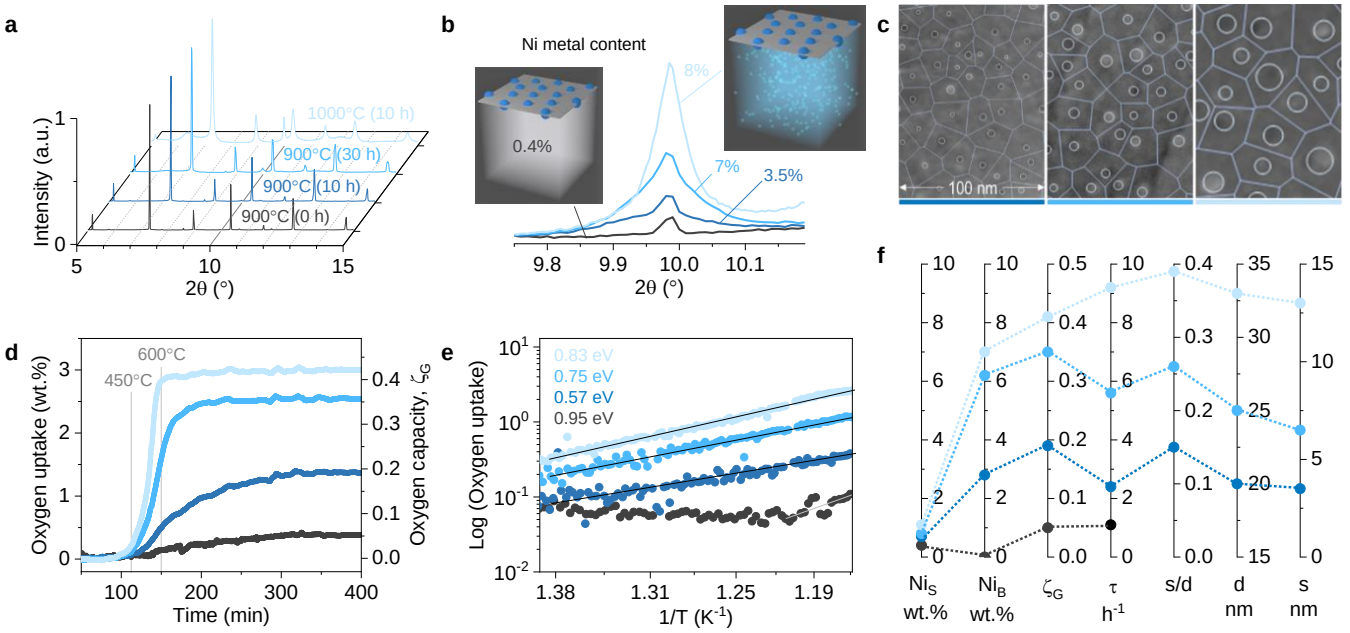

Figure 3. Controlling bulk exsolution, strain and oxygen exchange. (**a**) Room temperature XRD of samples reduced at 900 °C for 0 h (dark grey), 10 h (dark blue) and 30 h (blue) and at 1000 °C for 10 h (light blue). (**b**) Detail of the Ni peak from **a** together with corresponding total (surface and bulk) Ni content (wt.%) calculated by Rietveld refinement. Schematic illustrations of samples without (left) and with (right) bulk particles. (**c**) SEM micrographs and calculated Voronoi tessellation of the spatial arrangement of embedded particles contained in the samples denoted in **a** by the blue range of colours. (**d**) Oxygen weight gain and corresponding oxygen capacity (mol O per mol of perovskite) as a function of time, up to a temperature of 600 °C, for the samples shown in **a**. (**e**) Arrhenius plot corresponding to the data shown in **d** together with the calculated activation energy for oxygen transport. (**f**) Parallel axes plot for the samples shown in **a** for the Ni metal content at the surface (Ni_S, wt.%) and in the bulk (Ni_B, wt.%) calculated from Rietveld refinement of the data from **a**, oxygen capacity (ζ_G, mol O per mol of perovskite), time constant of oxygen exchange calculated from the data shown in **d** (τ, h^{-1}, see Fig. S8), ratio of the average bulk particle diameter (s) and average distance between neighbouring bulk particles (d), average bulk particle diameter (s, nm) and average distance between neighbouring bulk particles (d, nm, see Fig. S7).

parameters related to the size and interparticle distance of the embedded particles, in particular, the ratio between these (compare τ and s/d in Fig. 3f). This is probably not surprising considering that such parameters are expected to be indicative of the degree of strain the particles exert over the host lattice. Nonetheless, an Arrhenius plot of the oxygen exchange data revealed that the activation energies for the oxygen transport are characteristic of perovskites, although generally much closer to values reported for perovskites with higher oxide ion diffusivities than titanates[38]. This indicates that while the perovskite is still responsible for mediating oxygen exchange between the surface and the embedded metal nanoparticles, its oxygen transport capabilities have been strongly enhanced by the introduction of strain via the embedded metal particles.

Further increase in strain through reversible oxygen incorporation

A way to further increase strain would be to take advantage of the different redox expansion of the perovskite phase and the embedded Ni phase[39]. That is, upon oxidation, the Ni lattice expands by about 15% due to oxygen incorporation. On the contrary, when oxygen is incorporated in the perovskite oxygen vacancies, this has minimal effect on lattice dimensions, which are, in turn, dominated by the increased charge of the B-site ions, leading to a net contraction of the unit cell of <1%[40].

In order to better understand the process of oxygen re-incorporation and further straining of the $rABO_3$ matrix, we monitor oxygen uptake by gas composition analysis as a function of temperature and correlate this with real time structural information via Rietveld refinement of synchrotron X-ray data (Fig. 4, S9).

From room temperature (RT) up to ~400 °C the system only undergoes thermal expansion (Fig 4a-e). The thermal expansion of Ni is consistent with literature values, 1.34 10^{-5} $°C^{-1}$ while the expansion of the $rABO_3$ matrix, 0.94 10^{-5} $°C^{-1}$, is characteristic of similar perovskite systems[41],[42], indicating that up to this temperature, they behave as individual phases.

Starting at 400 °C, the Ni phase begins to oxidise, as evidenced by a decrease in its fraction from 8 to 4 wt.%. At around 550 °C, the slope in the expansion of the unit cell of the perovskite increases. This is, however, counterintuitive because the residual (stoichiometric) perovskite lattice is expected to contract upon oxidation[40,43]. Thus, it appears that the lattice expansion from Ni to NiO accounts for the observed lattice expansion of the perovskite, demonstrating that the two phases now behave as if connected. Most notable, though, within the same temperature window, the degree of microstrain in the $rABO_3$ matrix increases dramatically, ~6 fold (Fig. 4d, S9), whilst maintaining the crystal and grain structure (Fig. S1, S10). The whole process is completed by 600 °C, with further increase in temperature not causing any additional structural changes. Analysis of the sample

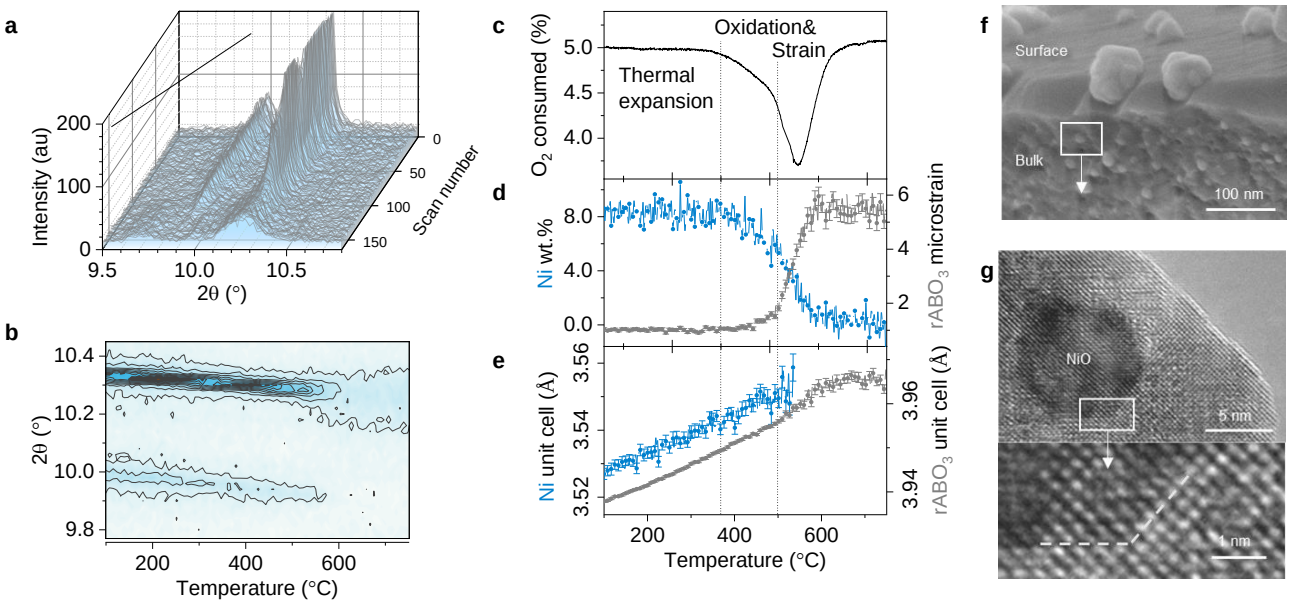

Figure 4. Increasing strain levels to unlock oxygen ion exchange. (**a**) XRD data acquired during the temperature programmed oxidation of a system with submerged nanoparticles presented in 3D plot as a function of diffraction angle, time and scan number. (**b**) XRD data from **a** presented in a 2D plot as a function of diffraction angle, time and corresponding temperature. (**c**) O_2 (%) consumption during experiment **a**. (**d**)-(**e**) structural information calculated from **a** by Rietveld refinement showing: (**d**) Ni metal content and $rABO_3$ microstrain (relative to the initial, reduced state value) as a function of time and temperature and (**e**) Unit cell parameter of the Ni metal and $rABO_3$ phase as a function of time and temperature. (**f**) Cross-section SEM image of the sample after the experiment described in **a**. (**g**) TEM image and close up detail of the sample after the experiment described in **a**, showing the crystallographic alignment between the perovskite and a NiO nanoparticle within it. The dotted line highlights the interface between the particle and the perovskite.

after this experiment indicated that all the Ni metal had been converted to NiO while still remaining socketed (Fig. 4d, 4f), the La_2TiO_5 phase remained unchanged (Fig. S1), and the crystallographic alignment between the bulk particles and the perovskite was preserved (Fig. 4g). It is worth noting that this dramatic increase in microstrain during the first oxidation experienced by the $rABO_3$ appears to be permanent, being maintained during additional redox cycles (Fig. S11) and causes a further 15% increase of the oxygen exchange time constant τ. Overall, this denotes that we have created a system with very high oxygen capacity which largely comes from the embedded Ni nanoparticles, while the strain that these particles induce is responsible for the fast oxygen exchange capabilities.

Using an endogenous nanoparticle system to activate methane

To demonstrate the utility of this system, we apply it to the challenging process of CH_4 activation, by monitoring methane conversion and selectivity as a function of temperature (Fig. 5). We compare, on a weight basis, our low surface area system (~1 $m^2\ g^{-1}$) having most particles enclosed in the bulk (Ni-$rABO_3$), against a high surface area (~100 $m^2\ g^{-1}$) Ni/Al_2O_3 with a similar loading of metal particles (10 wt.%, ~8 nm size, Fig. S12), which are instead located on the surface (state-of-the-art for methane conversion[44]).

The Ni-$rABO_3$ system activates CH_4 in a narrow temperature window, with a sharp consumption peak at 550 °C, followed by a broader peak at 600 °C, selectively yielding syngas with a H_2:CO 2:1 ratio, ideal for synthetic fuel production (Fig. 5a-b)[45]. The reference sample displays a similar CH_4 activation profile, starting 50 °C higher (in spite of the large surface area and thus availability of active sites), while only the first sharp peak corresponds to oxygenated gaseous products (albeit being less selective, Fig. 5a-b). The second peak, spreading over a 100 °C temperature window, corresponds exclusively to CH_4 cracking (Fig. S13). This indicates that in Ni/Al_2O_3, once the NiO has been converted to Ni metal particles these become active sites for carbon deposition[44]. On the contrary, in the exsolved system, due to the confined and aligned nature of the metallic Ni particles, this mechanism is not favoured, consistent with previous observations whereby exsolved particles are able to supress coke in hydrocarbon environments[13].

Consequently, the Ni-$rABO_3$ is almost exclusively selective towards syngas (87%) while Ni/Al_2O_3 demonstrates overall 88% selectivity towards carbon deposition.

The outstanding behaviour of the submerged particle system under reaction conditions seems to stem from synergistic contribution of its components. In order to deconvolute this, two variations of our system were prepared and tested. Firstly, a system where surface particles were removed, keeping the ones in the bulk intact, showed no activity, (P1 in Fig. 5a), indicating that the presence of confined surface particles is essential to enable coke-free methane activation (Fig. 5d). Secondly, a system only having surface particles was also inactive in this

temperature window (P2, Fig. 5a) indicating that in absence of sufficient oxygen capacity, the surface particles alone are not

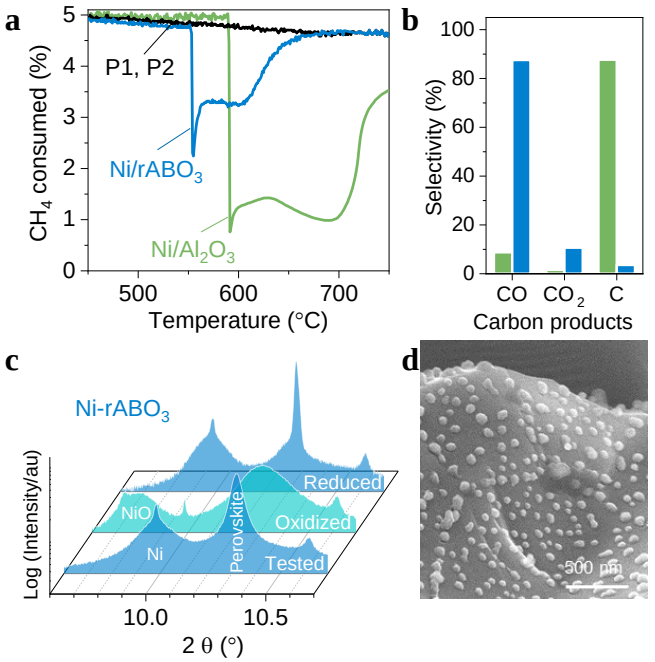

Figure 5. Using submerged nanoparticle system to activate methane. (**a**) Methane consumption as a function of temperature for various systems (150 mg) : Ni/Al_2O_3 (green) (SSA ~ 100 m^2/g), a system with surface and bulk exsolved particles, Ni-$rABO_3$ (blue) (SSA ~ 1 m^2/g) containing nanoparticles exsolved at the surface and within the bulk, and P1 and P2 (black), representative of a sample with only surface particles and one with only bulk particles (all surface particles were etched), respectively. (**b**) Selectivity over carbon-containing products corresponding to the experiment described in **a**. (**c**) Room temperature XRD data for Ni-$rABO_3$ at different stages: fresh (i.e. reduced), after oxidation and after testing for CH_4 activation in the experiment described in **a**. (**d**) SEM image of the surface after the experiment described in **a**.

enough to promote CH_4 conversion. However, when both surface and bulk particles are present (Ni-$rABO_3$), they operate in tandem and all the submerged NiO particles (located as deep as tens of µm under the surface) are being used and converted to Ni metal during the catalytic transformation of CH_4 to syngas, as evidenced by XRD (Fig. 5c). In fact, the phase change from NiO to Ni accounts for 85% of the conversion to oxygenated products, the remaining being due to the oxygen capacity of the $rABO_3$ matrix. Last but not least, the $rABO_3$ matrix is capable of efficiently mediating O transfer between the embedded particles and the surface-activated CH_4 due to its strain-induced functionality. This is also apparent from comparing the activity of systems with various embedded nanoparticle content which shows that conversion generally increases with increasing amount of embedded nanoparticles and thus with potential bulk strain, as given by the s/d parameter (see Fig. 3 and S7e). As shown above, in reduced state, the metallic nanoparticles experience expansive strain, while in oxidised state (required for methane conversion), it is the perovskite that experiences expansive strain (the unit cell parameter of NiO is larger than that of the perovskite by ~7%). Expansive (or tensile) strain has been previously shown to enhance oxygen exchange considerably[46]. Additionally, the introduction of embedded nanoparticles also enhances the oxygen vacancy content of the support oxide material which is also expected to contribute towards enhanced oxygen exchange (see Supplementary Note 2). Thus, it seems that our system behaves kinetically as if all the NiO particles are on the surface, yet because they are actually submerged in the perovskite matrix, this allows for controlled release of the oxygen in order to selectively produce syngas[47].

Operando mechanistic insight of CH_4 conversion with endogenous particles

In order to gain a better understanding of how the above-mentioned components of the system operate during CH_4 conversion, we monitor this process operando, combining gas composition analysis with real time structural information via Rietveld refinement of synchrotron X-ray data (Fig. 6, S14). Based on this we identify five stages in this process (Fig. 6b, 6g). Firstly, from RT to 500 °C the system only seems to undergo thermal expansion, with seemingly uncorrelated thermal expansion coefficients of the two phases (~1.06 10^{-5} and ~1.29 10^{-5} $°C^{-1}$ for $rABO_3$ and NiO, respectively)[42].

In the second stage, methane activation is initiated through a sharp CH_4 consumption peak at ~550 °C. This coincides with a decrease in the NiO fraction from ~10.3 to 9 wt.% which corresponds to the amount of NiO we have shown to be on the surface (Fig. 3f). Therefore, it seems that the initial sharp CH_4 peak is mostly due to the surface particles being reduced, which is probably not surprising considering that the Ni/Al_2O_3 system exhibits a similar initial peak. In this stage, the unit cell parameter of the $rABO_3$ matrix also rises sharply, indicating it is being reduced by CH_4. This process is probably facilitated by the newly formed surface Ni metal particles which activate CH_4, with the perovskite supplying the O^{2-} ions (Eq. 1). Consequently, this leaves vacancies in the perovskite lattice (Eq. 2) which enable hopping sites for oxygen to be transported and, at the same time, the electrons released in the perovskite lattice will decrease the oxidation state of the B-site ions (Eq. 3), expanding the unit cell.

$$CH_4 + O^{2-} \longrightarrow CO + 2H_2 + 2e^- \quad \text{(Eq. 1)}$$

$$O_O^x \longrightarrow O^{2-} + V_O^{\cdot\cdot} \quad \text{(Eq. 2)}$$

$$e^- + B_B^x \longrightarrow B_B' \quad \text{(Eq. 3)}$$

In the third stage, which spans a time/temperature window of 10 minutes/ 50 °C, respectively, the unit cell of the perovskite remains relatively constant while the submerged NiO nanoparticles are being gradually converted to Ni metal. During this stage CH_4 is almost exclusively converted to syngas (H_2:CO 2:1, Fig. 6b). The fact that the $rABO_3$ unit cell does not change during this stage is rather intriguing considering that it should increase due to further reduction or, most importantly, due to

continued thermal expansion. This seems to imply that the dramatic lattice contraction that accompanies the transformation of NiO to Ni (15%) greatly affects the perovskite lattice, counterbalancing and negating its thermal expansion.

Therefore, as opposed to the first stage dominated by seemingly uncorrelated thermal expansion, under reaction conditions the system works in a concerted manner.

In the fourth stage, starting once all the bulk NiO has been used, there is an increase in the slope of the $rABO_3$ unit cell which is larger than the one observed in the thermal expansion stage, indicating that the perovskite is now being slightly reduced and assisting with the conversion of a small, final amount of CH_4. Once this is completed, the slope of the unit cell of the perovskite reverts to the value corresponding to thermal expansion.

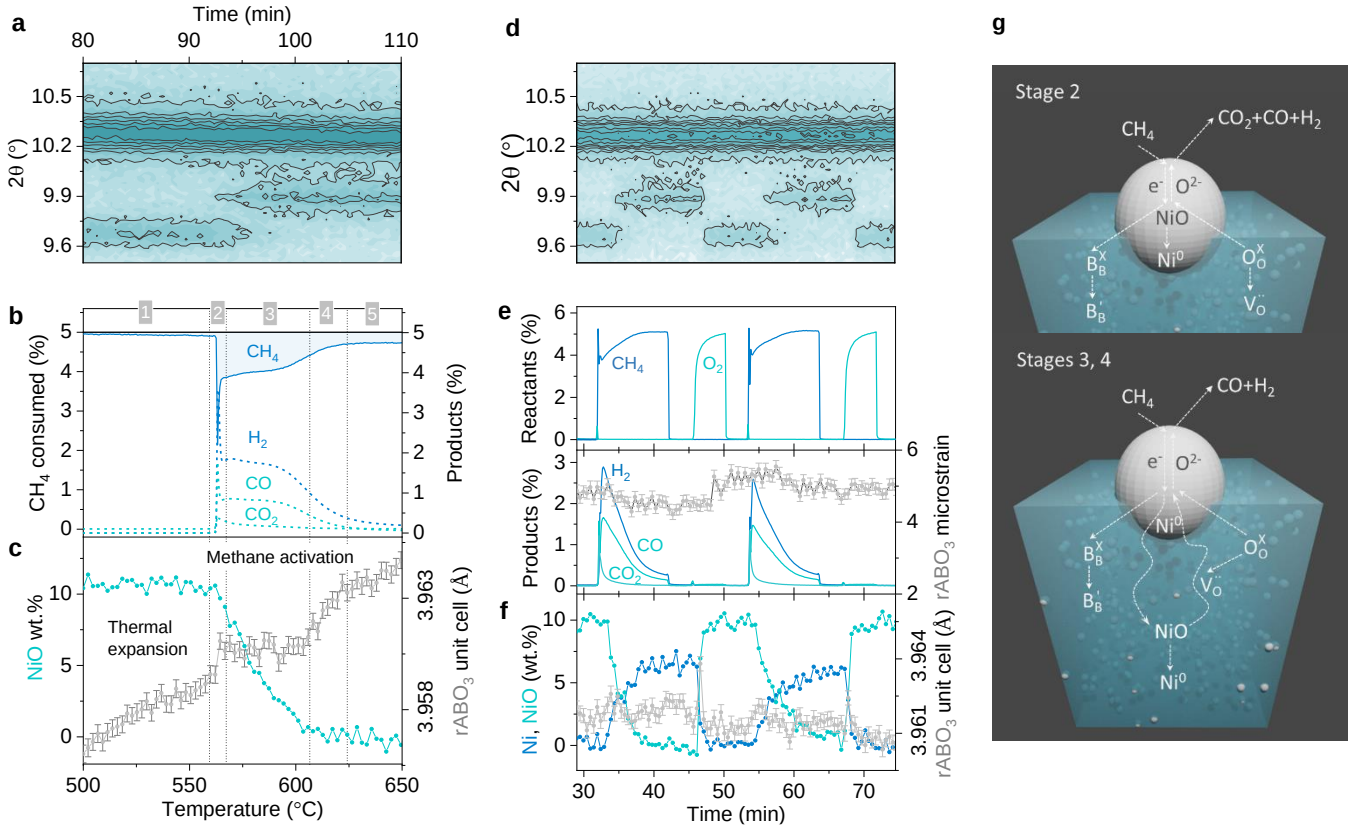

Figure 6. Operando mechanistic insight into CH_4 conversion with submerged nanoparticles. (**a**) XRD data acquired during the temperature programmed reduction under 5% CH_4 of a system with submerged nanoparticles presented as 2D plot, as a function of diffraction angle, time and corresponding temperature. (**b**) CH_4 consumed and corresponding H_2, CO_2, CO produced during the experiment described in **a**. (**c**) NiO content and perovskite unit cell parameter calculated from **a** by Rietveld refinement and plotted as a function of time and temperature. (**d**) 2D plot of the XRD pattern of the material in operando while cycling the material between redox feeds at 650 °C. (**e**) CH_4, O_2, H_2, CO, CO_2 gas composition at the outlet during experiment described in **d** and $rABO_3$ microstrain during cycling calculated from Rietveld refinement. (**f**) Ni and NiO content and perovskite unit cell parameter calculated from **d** by Rietveld refinement and plotted as a function of time. (**g**) Schematic of methane conversion mechanism corresponding to the main stages identified from **a**.

In view of potential applicability, we monitor the catalytic, redox performance and structure in operando during cycling (Fig. 6d-f). We choose to do this at 650 °C, which is at the end of the activity temperature window identified by the experiment shown in Fig. 6b. For the reduction (CH_4) cycle we used a length of 10 minutes and for the oxidation cycle (O_2) 5 minutes. This experiment revealed that the system reversibly operates in a coke-free, highly selective manner, showing no signs of mechanical degradation (e.g. cracks) that normally occur in composites under cycling (Fig. S15). Based on the structural changes identified from the Rietveld refinement of the data, the oxidation of the system is very fast, occurring in less than 1 minute, while the reduction was slower, typically being completed in about 6 minutes (Fig. 6f). Additionally, the phase analysis shown in Fig 6f indicates that the embedded particles are being cycled between reduced and oxidised state and do not redissolve into the perovskite upon oxidation because the fraction of the NiO remains constant and equal to the starting value upon consecutive redox cycles. Moreover, throughout this cyclic transformation the perovskite matrix remains strained to the same levels induced by the first oxidation (Fig 4d, 6e).

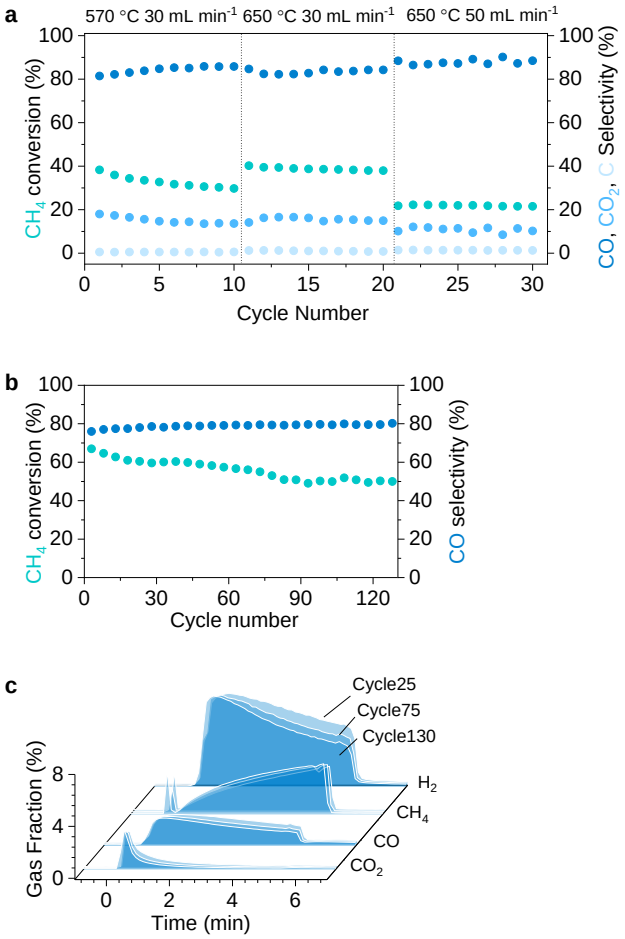

Figure 7. Long term stability. (**a**)-(**b**) Conversion and selectivity as a function of cycle number, during CH_4 conversion to syngas using submerged nanoparticle system (**a**) at different temperatures and flow rates, using 150 mg of sample. (**b**) at 570 °C and 30 mL min^{-1} (NTP), using 300 mg of sample, over 130 cycles. (**c**) Outlet gas composition versus time in 3 representative cycles from experiment **b**.

Application and long-term durability

In order to better understand the potential application of the system, we employ chemical looping partial oxidation of CH_4 (CLPO). We test the system under different conditions to identify suitable operating conditions (Fig. 7a). We choose two temperatures, 570 and 650 °C, corresponding to the middle and end of the temperature activity window identified above (Fig. 6b). We also change the contact time in order to monitor its effect on the activity and selectivity of the system.

Since the selectivity is seemingly mediated by the embedded particles and both temperatures are enough to enable oxygen exchange to access them, CO selectivity varies from 80 to 90%, proving that regardless of the operating conditions, our system remains highly selective to the desired products. As expected, the conversion seems to be higher at higher temperature and longer contact times. In all cases, the selectivity towards carbon deposition was lower than 1%.

In order to test long term stability and cyclability, we use double the amount of material (300 mg) than in the previous experiments

and we operate our system at 570 °C and 30 mL min^{-1} (NTP). In these conditions, we observe that selectivity remains stable over 130 cycles at >80%, while the conversion starts at 70% and stabilizes at 55% after 90 cycles (Fig. 7b-c), while carbon depositions remains <1% (Fig. S16). At the same time, after this extensive cycling, the overall microstructure of the composite is retained while the average size of the embedded particles increases slightly by about 10% and some of the smallest nanoparticles (<5 nm) seem to have disappeared (see Fig. S16). As compared to the literature, where similar mass to flow rate ratios were used, our system achieves similar conversion and selectivity, at a temperature on average of 300 °C lower, and, generally, over a larger number of cycles demonstrating better overall stability[30,48,49].

Conclusion

The results presented above vividly illustrate the extensive, homogenous and controlled endogenous growth of metallic nanoparticles at nanoscale proximity within perovskite oxides. The hierarchical nature of this system shares strong parallel with substitutional doping of materials[11]. Just like doping has been revolutionary in controlling an extensive array of material properties, bulk nanocluster “doping” of oxides could provide an entirely new dimension to tailor hierarchically nanostructured materials and their emergent functionality. However, as opposed to substitutional doping which maintains the continuity of the host lattice, changing its local or extended chemical structure, the nanocluster insertion causes both physical and chemical disruption of the host lattice, inducing local strain and forming new interfaces within the host lattice, offering new opportunities for strain and interface engineering of materials.

By growing a high population of nanoparticles throughout the oxide, we simultaneously induce strain throughout both phases, greatly enhancing oxygen transport and exchange as well as overall system reactivity. This is consistent with previous reports showing that expansive strain assists with reversible oxygen incorporation/release[3] while a degree of 1% strain (in our case 0.37% for the bulk particles) increases catalytic reactivity by up to 300%[6,9]. Such strain-enhanced oxygen transport could be exploited in many fields including, but not limited to, oxide ion transport membranes, electrolytes or electrodes.

The large fraction of embedded-metal phase means that the system displays a very large oxygen storage capacity (about one order of magnitude higher than conventional perovskites[48]), which is important in fields such as chemical looping, thermochemical solar to fuels conversion or three way catalysts and the reversibility over such a large number of cycles demonstrated here unlocks new ways of stabilising

nanocomposites (cermets) for redox cycling applications[30]. On the other hand, the ability to disperse metal nanoparticles within oxides could enable new opportunities in the design of magnetic or thermoelectric materials.

Finally, the combined effect of high oxygen storage capacity and fast, reversible oxygen release/incorporation enable even the deepest embedded particles to be accessible to the gas stream. This, coupled with surface active sites, has enabled to bypass conventional degradation and poisoning mechanisms and tackle challenging catalytic transformations such as CH_4 conversion to syngas.

Acknowledgements

We acknowledge the support of the European Synchrotron Radiation Facility (ESRF) for experiment no. MA-4239. We would like to thank Dr. Catherine Dejoie for her valuable help during data acquisition at beamline ID22. We also thank Dr Budhika Mendis for access to Durham University Microscopy Facility. The research leading to these results has received funding from the European Research Council under the European Union's Seventh Framework Programme (FP/2007-2013) / ERC Grant Agreement Number 320725 and from the EPSRC via grants EP/P007767/1, EP/P024807/1, EP/R023921/1.

The raw data supporting this publication are available at 10.25405/data.ncl.11302853.

Keywords: exsolution, strain, oxygen exchange/ capacity, methane conversion, chemical looping

[1] S. J. Kim, T. Akbay, J. Matsuda, A. Takagaki, T. Ishihara, *ACS Applied Energy Materials* **2019**, *2*, 1210–1220.
[2] M. Cargnello, A. C. Johnston-Peck, B. T. Diroll, E. Wong, B. Datta, D. Damodhar, V. V. T. Doan-Nguyen, A. A. Herzing, C. R. Kagan, C. B. Murray, *Nature* **2015**, *524*, 450–453.
[3] J. Greeley, W. P. Krekelberg, M. Mavrikakis, *Angewandte Chemie International Edition* **2004**, *43*, 4296–4300.
[4] Y. Wu, Z. Chen, P. Nan, F. Xiong, S. Lin, X. Zhang, Y. Chen, L. Chen, B. Ge, Y. Pei, *Joule* **2019**, *3*, 1276–1288.
[5] E.-M. Choi, A. D. Bernardo, B. Zhu, P. Lu, H. Alpern, K. H. L. Zhang, T. Shapira, J. Feighan, X. Sun, J. Robinson, et al., *Science Advances* **2019**, *5*, eaav5532.
[6] P. Strasser, S. Koh, T. Anniyev, J. Greeley, K. More, C. Yu, Z. Liu, S. Kaya, D. Nordlund, H. Ogasawara, et al., *Nature Chemistry* **2010**, *2*, 454–460.
[7] L. Wang, Z. Zeng, W. Gao, T. Maxson, D. Raciti, M. Giroux, X. Pan, C. Wang, J. Greeley, **2019**, 6.
[8] H. Jalili, J. W. Han, Y. Kuru, Z. Cai, B. Yildiz, *J. Phys. Chem. Lett.* **2011**, *2*, 801–807.
[9] M. Escudero-Escribano, P. Malacrida, M. H. Hansen, U. G. Vej-Hansen, A. Velázquez-Palenzuela, V. Tripkovic, J. Schiøtz, J. Rossmeisl, I. E. L. Stephens, I. Chorkendorff, *Science* **2016**, *352*, 73–76.
[10] P. Lu, X. Wu, W. Guo, X. C. Zeng, *Phys. Chem. Chem. Phys.* **2012**, *14*, 13035–13040.
[11] L. De Rogatis, M. Cargnello, V. Gombac, B. Lorenzut, T. Montini, P. Fornasiero, *ChemSusChem* **2010**, *3*, 24–42.
[12] D. Neagu, E. I. Papaioannou, W. K. W. Ramli, D. N. Miller, B. J. Murdoch, H. Ménard, A. Umar, A. J. Barlow, P. J. Cumpson, J. T. S. Irvine, et al., *Nature Communications* **2017**, *8*, DOI 10.1038/s41467-017-01880-y.
[13] D. Neagu, T.-S. Oh, D. N. Miller, H. Ménard, S. M. Bukhari, S. R. Gamble, R. J. Gorte, J. M. Vohs, J. T. S. Irvine, *Nature Communications* **2015**, *6*, DOI 10.1038/ncomms9120.
[14] S. Liu, Q. Liu, J.-L. Luo, *ACS Catal.* **2016**, *6*, 6219–6228.
[15] J. T. S. Irvine, D. Neagu, M. C. Verbraeken, C. Chatzichristodoulou, C. Graves, M. B. Mogensen, *Nature Energy* **2016**, *1*, 15014.
[16] N. W. Kwak, S. J. Jeong, H. G. Seo, S. Lee, Y. Kim, J. K. Kim, P. Byeon, S.-Y. Chung, W. Jung, *Nature Communications* **2018**, *9*, 4829.
[17] Y. Zhu, W. Zhou, R. Ran, Y. Chen, Z. Shao, M. Liu, *Nano Lett.* **2016**, *16*, 512–518.
[18] O. Kwon, S. Sengodan, K. Kim, G. Kim, H. Y. Jeong, J. Shin, Y.-W. Ju, J. W. Han, G. Kim, *Nature Communications* **2017**, *8*, 15967.
[19] D. Zubenko, S. Singh, B. A. Rosen, *Applied Catalysis B: Environmental* **2017**, *209*, 711–719.
[20] Y. Gao, J. Wang, Y.-Q. Lyu, K. Lam, F. Ciucci, *J. Mater. Chem. A* **2017**, *5*, 6399–6404.
[21] R. Thalinger, M. Gocyla, M. Heggen, R. Dunin-Borkowski, M. Grünbacher, M. Stöger-Pollach, D. Schmidmair, B. Klötzer, S. Penner, *Journal of Catalysis* **2016**, *337*, 26–35.
[22] R. Michalsky, V. Botu, C. M. Hargus, A. A. Peterson, A. Steinfeld, *Advanced Energy Materials* **2015**, *5*, 1401082.
[23] N. Xu, X. Li, X. Zhao, J. B. Goodenough, K. Huang, *Energy Environ. Sci.* **2011**, *4*, 4942–4946.
[24] I. S. Metcalfe, B. Ray, C. Dejoie, W. Hu, C. Leeuwe, C. Dueso, F. Garcia-Garcia, C.-M. Mak, E. I. Papaioannou, C. Thompson, et al., *Nature Chemistry* **n.d.**, DOI https://doi.org/10.1038/s41557-019-0273-2.
[25] P. Tang, Q. Zhu, Z. Wu, D. Ma, *Energy Environ. Sci.* **2014**, *7*, 2580–2591.
[26] B. Christian Enger, R. Lødeng, A. Holmen, *Applied Catalysis A: General* **2008**, *346*, 1–27.
[27] A. Thursfield, A. Murugan, R. Franca, I. S. Metcalfe, *Energy Environ. Sci.* **2012**, *5*, 7421–7459.
[28] S. Chen, L. Zeng, H. Tian, X. Li, J. Gong, *ACS Catal.* **2017**, *7*, 3548–3559.
[29] K. Li, H. Wang, Y. Wei, "Syngas Generation from Methane Using a Chemical-Looping Concept: A Review of Oxygen Carriers," DOI 10.1155/2013/294817can be found under https://www.hindawi.com/journals/jchem/2013/294817/, **2013**.
[30] L. Zeng, Z. Cheng, J. A. Fan, L.-S. Fan, J. Gong, *Nature Reviews Chemistry* **2018**, *2*, 349–364.
[31] R. Merkle, J. Maier, *Angewandte Chemie International Edition* **2008**, *47*, 3874–3894.
[32] L. Qin, M. Guo, Y. Liu, Z. Cheng, J. A. Fan, L.-S. Fan, *Applied Catalysis B: Environmental* **2018**, *235*, 143–149.
[33] S. Miyoshi, M. Martin, *Phys. Chem. Chem. Phys.* **2009**, *11*, 3063–3070.
[34] T.-S. Oh, E. K. Rahani, D. Neagu, J. T. S. Irvine, V. B. Shenoy, R. J. Gorte, J. M. Vohs, *The Journal of Physical Chemistry Letters* **2015**, *6*, 5106–5110.
[35] Y. Gao, D. Chen, M. Saccoccio, Z. Lu, F. Ciucci, *Nano Energy* **2016**, *27*, 499–508.
[36] S. Cho, C. Yun, S. Tappertzhofen, A. Kursumovic, S. Lee, P. Lu, Q. Jia, M. Fan, J. Jian, H. Wang, et al., *Nature Communications* **2016**, *7*, 12373.
[37] J. L. MacManus-Driscoll, P. Zerrer, H. Wang, H. Yang, J. Yoon, A. Fouchet, R. Yu, M. G. Blamire, Q. Jia, *Nature Materials* **2008**, *7*, 314–320.
[38] R. A. De Souza, *Advanced Functional Materials* **2015**, *25*, 6326–6342.
[39] K. Yuan, S. S. Lee, W. Cha, A. Ulvestad, H. Kim, B. Abdilla, N. C. Sturchio, P. Fenter, *Nature Communications* **2019**, *10*, DOI 10.1038/s41467-019-08470-0.
[40] S. R. Bishop, D. Marrocchelli, C. Chatzichristodoulou, N. H. Perry, M. B. Mogensen, H. L. Tuller, E. D. Wachsman, *Annual Review of Materials Research* **2014**, *44*, 205–239.
[41] O. Madelung, U. Rössler, M. Schulz, Eds. , in *Non-Tetrahedrally Bonded Binary Compounds II*, Springer Berlin Heidelberg, Berlin, Heidelberg, **2000**, pp. 1–4.
[42] D. Neagu, J. T. S. Irvine, *Chemistry of Materials* **2010**, *22*, 5042–5053.
[43] R. Moreno, J. Zapata, J. Roqueta, N. Bagués, J. Santiso, *J. Electrochem. Soc.* **2014**, *161*, F3046–F3051.
[44] C. Papadopoulou, H. Matralis, X. Verykios, in *Catalysis for Alternative Energy Generation* (Eds.: L. Guczi, A. Erdôhelyi), Springer New York, New York, NY, **2012**, pp. 57–127.
[45] D. Pakhare, J. Spivey, *Chem. Soc. Rev.* **2014**, *43*, 7813–7837.
[46] M. Kubicek, Z. Cai, W. Ma, B. Yildiz, H. Hutter, J. Fleig, *ACS Nano* **2013**, *7*, 3276–3286.
[47] O. Mihai, D. Chen, A. Holmen, *Journal of Catalysis* **2012**, *293*, 175–185.
[48] X. Zhu, K. Li, L. Neal, F. Li, *ACS Catalysis* **2018**, *8*, 8213–8236.
[49] X. P. Dai, R. J. Li, C. C. Yu, Z. P. Hao, *The Journal of Physical Chemistry B* **2006**, *110*, 22525–22531.

Controlled growth of metallic nanoparticles at the surface and bulk of perovskite oxides induce strain and promote oxygen exchange with a methane stream leading to syngas production.

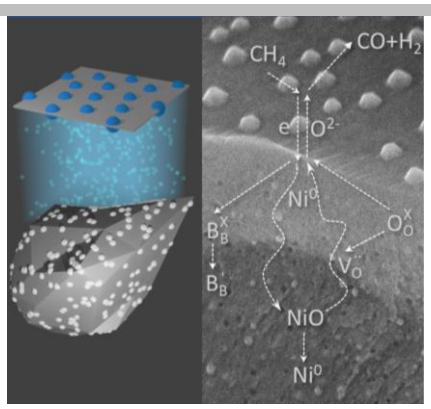

Kalliopi Kousi, Dragos Neagu,* Leonidas Bekris, Evangelos I. Papaioannou and Ian S. Metcalfe*

Page No. – Page No.

Endogenous Nanoparticles Strain Perovskite Host Lattice Providing Oxygen Capacity and Driving Oxygen Exchange and CH_4 Conversion to Syngas